2021 EAGE ANNUAL
82ND CONFERENCE & EXHIBITION
AMSTERDAM | THE NETHERLANDS

LAND FWI: CHALLENGES AND POSSIBILITIES

D. Wang[1], C. Chen[1], D. Zhuang[1], J. Mei[1], P. Wang[1]

[1] CGG

Summary

Land seismic presents more and different challenges for Full-Waveform Inversion (FWI) than marine data. Among these challenges, the most fundamental ones are the irregular topography, strong near-surface effects, and common FWI difficulties such as cycle-skipping and amplitude issues. In this work, we propose to deploy three strategies to deal with these difficulties respectively: curvilinear topography modelling to effectively model the irregular topography for the earth's surface, mitigation of near-surface effects to reduce the negative impacts of strong near-surface noise, and a stable cost function as the foundation for land FWI to alleviate cycle-skipping and amplitude issues. We demonstrate the effectiveness of our strategies with two field data examples representing different geological settings. Based on learnings from these studies, we believe that land FWI is becoming more stable and consistent than before, and success can be expected on more land datasets.

Introduction

Full-Waveform Inversion (FWI) promises automatic velocity model building (Tarantola, 1984) by using the full waveform of seismic data to iteratively update the earth parameters in a fashion that minimizes the misfit between observed data and modelled data. Recent advances in FWI (e.g., Shen et al., 2017; Zhang et al., 2018) have made it an essential tool for velocity model building, and now it is routinely applied (Wang et al., 2019) on industry-scale projects. However, the success of FWI has mainly been limited to marine datasets, which usually have the benefits of high signal-to-noise ratio (S/N), low frequencies and long offsets, in addition to a simple near-surface water layer. There are much fewer successes on land seismic data (Plessix et al., 2010; Mei and Tong, 2015; Sedova et al., 2017), and such successful examples are often case-specific. The experiences gained from these case studies are difficult to extend to other geological settings. This is understandable because land seismic presents more and different challenges for FWI than marine data. Among these challenges, we believe the most fundamental ones are: 1) an irregular topography, which is difficult to model; 2) strong near-surface effects due to the highly complex shallow earth layer; and 3) common FWI difficulties such as cycle-skipping and amplitude issues.

We propose three strategies to deal with the afore-mentioned difficulties, respectively: 1) use curvilinear coordinates for the topography modelling; 2) mitigate near-surface effects by attenuating them on both input and synthetic data; and 3) apply a stable FWI cost function to alleviate cycle-skipping and amplitude issues. In the next sections, we describe our methodology in detail and demonstrate the effectiveness of our strategies with field data examples.

Methodology

Strategy #1: Curvilinear topography modelling

Land seismic data is typically acquired on a non-flat topography with irregular elevation variations, so an accurate and efficient modelling of the topography is desired for land FWI. The curvilinear coordinate modelling method (Shragge, 2014) has shown to be effective in modelling topography and is the method we employed in this study. Here we use the isotropic (ISO) second-order acoustic wave equation to illustrate this method. In the regular Cartesian coordinate system, the ISO wave equation takes the form:

$$\left(\frac{1}{v^2}\frac{\partial^2}{\partial t^2} + \left(\sqrt{\rho}\nabla_x{}^2\frac{1}{\sqrt{\rho}}\right) - \nabla_x{}^2\right)u = \mathcal{F}_x\,, \tag{1}$$

where the subscript x denotes the Cartesian coordinate system (x_1, x_2, x_3) and v, ρ the velocity and density. In this coordinate system, the topography does not necessarily align with the modelling grid (Figure 1) and the conventional finite-difference method often generates artefacts such as staircase scattering. To overcome this, a curvilinear coordinate transform is performed according to

$$\begin{pmatrix}\xi_1\\ \xi_2\\ \xi_3\end{pmatrix} = \begin{pmatrix}x_1\\ x_2\\ a\cdot\left(\frac{x_3-\tau}{a-\tau}\right)\end{pmatrix}, \tag{2}$$

where $\tau = \tau(x_1, x_2)$ denotes the topography surface and a is a reference depth down to which the transform is performed. After this transformation, the topography becomes flat and evenly sampled in the new modelling grid (Figure 1), and the conventional finite-difference method can naturally be applied. In the transformed coordinate system, the wave equation takes a new form:

$$\left(\frac{1}{v^2}\frac{\partial^2}{\partial t^2} + \left(\sqrt{\rho}\nabla_\xi{}^2\frac{1}{\sqrt{\rho}}\right) - \nabla_\xi{}^2\right)u = \mathcal{F}_\xi\,, \tag{3}$$

where the scalar fields v, ρ and source $\mathcal{F}$ follow a simple point-to-point transform, while the differential operator $\nabla_\xi{}^2$ needs to be modified. Following the recipe described by Shragge (2014), we can reach

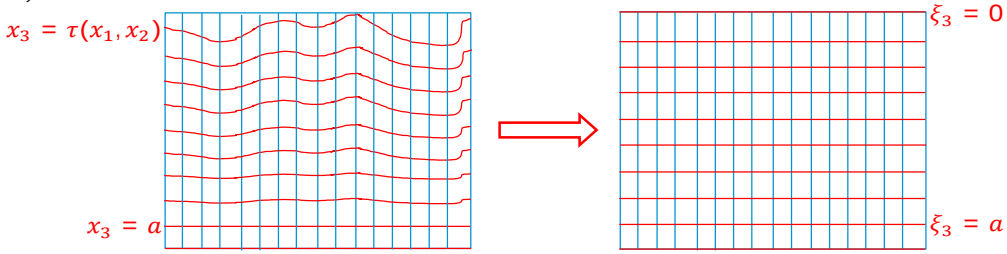

Figure 1 *Curvilinear coordinate transform.*

$$\nabla_\xi^2 = \zeta^i \frac{\partial}{\partial \xi_i} + g^{ij} \frac{\partial^2}{\partial \xi_i \partial \xi_j}, \quad (4)$$

where $\zeta^1 = \zeta^2 = 0, \zeta^3 = \frac{\xi_3 - a}{(a-\tau)^2}\left[(a-\tau)\left(\frac{\partial^2 \tau}{\partial {\xi_1}^2} + \frac{\partial^2 \tau}{\partial {\xi_2}^2}\right) + 2\left(\frac{\partial \tau}{\partial \xi_1}\right)^2 + 2\left(\frac{\partial \tau}{\partial \xi_2}\right)^2\right]$,

$g^{11} = g^{22} = 1,\ g^{33} = \left(\frac{a}{a-\tau}\right)^2 + \left(\frac{a-\xi_3}{a-\tau}\right)^2 \left[\left(\frac{\partial \tau}{\partial \xi_1}\right)^2 + \left(\frac{\partial \tau}{\partial \xi_2}\right)^2\right]$,

$g^{12} = g^{21} = 0, g^{13} = g^{31} = -\frac{a-\xi_3}{a-\tau}\frac{\partial \tau}{\partial \xi_1}, g^{23} = g^{32} = -\frac{a-\xi_3}{a-\tau}\frac{\partial \tau}{\partial \xi_2}$.

Here and after we follow the Einstein summation convention, where a twice-repeated index variable in a term means summation of that term over all the index values. After the wavefield is modelled in the curvilinear coordinate system according to Equations 3-4, it can be brought back to the physical domain using the reverse transform of Equation 2 for the gradient computation and the FWI update. This scheme can easily be extended to VTI and TTI modelling, in which the first- and second-order partial derivatives can be calculated according to

$$\frac{\partial}{\partial x_i} = \frac{\partial \xi_j}{\partial x_i}\frac{\partial}{\partial \xi_j}, \text{and } \frac{\partial^2}{\partial x_i \partial x_j} = \frac{\partial \xi_l}{\partial x_i}\frac{\partial \xi_m}{\partial x_j}\frac{\partial^2}{\partial \xi_l \partial \xi_m} + \frac{\partial^2 \xi_l}{\partial x_i \partial x_j}\frac{\partial}{\partial \xi_l}. \quad (5)$$

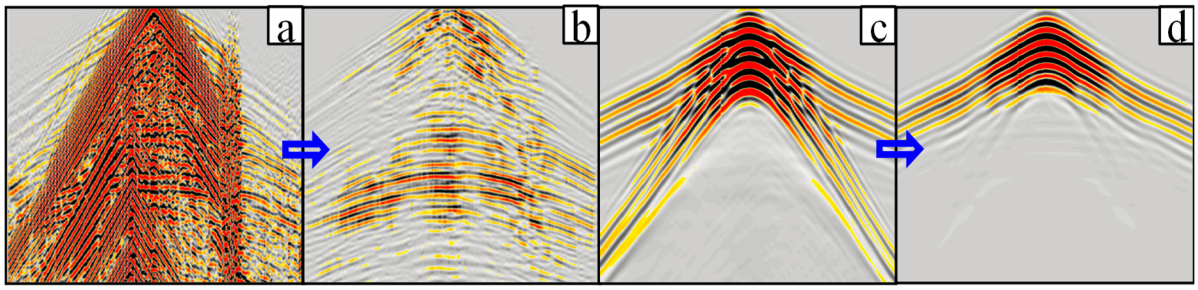

Figure 2 *Example of data shot gather: (a) before noise attenuation, (b) after noise attenuation; example of synthetic shot gather from the initial model: (c) without shallow wavefield attenuation, (d) with shallow wavefield attenuation.*

Strategy #2: Mitigation of near-surface effects

The highly complex near-surface layer poses another major challenge for land FWI, as it results in strong surface wave energy that usually overwhelms seismic records (Figure 2a). To mitigate the impact of this surface wave noise, we applied a dedicated noise attenuation (Le Meur et al., 2008) to bring out the diving and reflection waves usable for FWI (Figure 2b). After noise attenuation, no further mutes were necessary to select particular arrivals for FWI.

In addition, the modelled data often contains direct-arrival-looking events (Figure 2c) that are not represented in the observed data, which can mislead the FWI update. These events correspond to wavefields traveling through the shallow layer and can be attenuated by empirically scaling down the near-surface wavefield at every modelling time step before going into the next time step. After this procedure, these strong energies become less dominant (Figure 2d) and their negative impacts on the FWI update are mitigated.

Strategy #3: A stable cost function

Besides the specific challenges due to land data characteristics, land FWI also shares the common difficulties faced by any FWI such as cycle-skipping and amplitude issues. In recent years, different cost functions have been developed that are less prone to cycle-skipping and can better handle amplitude mismatches. Two examples of such methods are the traveltime-based cost function (i.e., TLFWI, Zhang et al., 2018) and the quadratic Wasserstein metric based cost function (i.e., W2FWI, Wang and Wang, 2019), both of which have been validated by various marine data examples. Although these methods were developed based on observations from marine seismic data, they can naturally be applied to land datasets. In the examples shown below, we used W2FWI as the inversion engine, but we want to point out that similar results, if not better, can be obtained with TLFWI as well.

Field data examples

We first applied the proposed method to a land dataset from the Permian Basin. The survey area is relatively flat with elevations ranging from 20 ft to 110 ft. This Vibroseis survey was acquired with a sweep from 4 to 90 Hz. The shot and receiver spacing was 150 ft by 750 ft and the maximum offset for

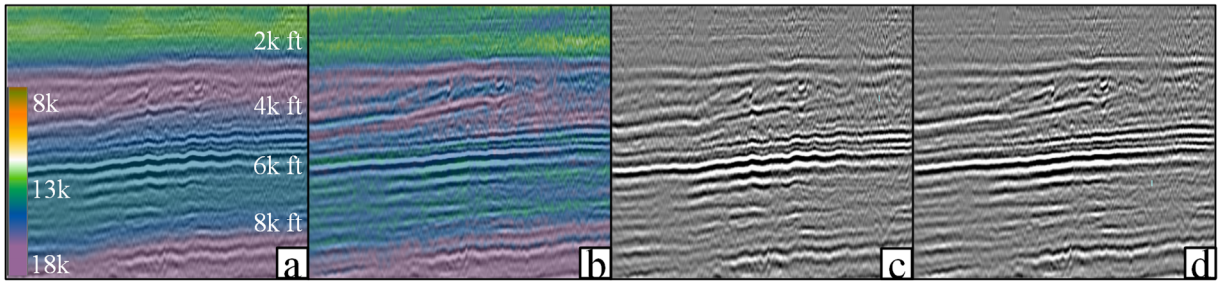

Figure 3 *Field data from the Permian Basin: Velocity model and Kirchhoff depth migration of (a)/(c) initial model and (b)/(d) FWI-updated model.*

the survey was about 20,000 ft. We used the Klauder wavelet as the source and ran FWI from 6 to 15 Hz; results are shown in Figure 3. We can see that with the initial velocity (Figure 3a), the migrated image (Figure 3c) contains a lot of undulations, especially noticeable for the strong reflectors in the middle section. FWI managed to correct the background velocity and added in detailed lateral variations to the model (Figure 3b), which flattened most of the undulations. As a result, the migration image (Figure 3d) has more simplified structures and the overall focusing of events is improved throughout the volume.

Next we look at an example from the Tabasco area located in the Alaska North Slope. This was also a Vibroseis survey with a sweep frequency from 4 to 80 Hz. Maximum offset for this survey was about 17,000 ft. The shot spacing was 27.5 ft by 550-660 ft and the receiver spacing was 110 ft by 990-1100 ft. This highly sparse and irregular spatial sampling added difficulties for FWI, especially in resolving the shallow velocity. A typical geological feature for this area is a fast-velocity permafrost layer followed by slower velocity layers (Figure 4d). This "velocity inversion" traps diving waves at a very shallow depth, so FWI needs to rely on reflections to update deep sections. In addition, the near-surface layer is highly heterogeneous with many ice lakes scattered around (Figure 4a). FWI was carried out on this data from 6 to 13 Hz. We observe that FWI correctly identified ice lakes (red arrows in Figures 4a and 4c) and positioned the base of the permafrost layer at a more accurate location (Figure 4f). Figures 5a-b show the stacked images and Figures 5c-d show the migrated gathers for the initial model and the FWI-updated model, respectively. The stacked image after FWI has better focusing, sharper faults, and simpler reflectors, and the gathers after FWI have improved event coherence and flatness.

Conclusions and discussions

We proposed an FWI method of three strategies targeting the major challenges in land seismic data: use of curvilinear topography modelling to effectively model the irregular topography of the earth's surface, mitigation of near-surface effects to reduce the negative impacts of strong near-surface noise, and implementation of a stable cost function to provide the foundation for land FWI to alleviate cycle-skipping and amplitude issues. The effectiveness of our method is demonstrated through two field data examples representing different geological contexts. The lessons learned indicate that land FWI is becoming more stable and consistent than before, and more FWI successes can be expected in the future.

In our land FWI workflow, we used an acoustic modelling engine to compute synthetic data, which is insufficient to represent the real world. Consequently, strategies such as mitigation of near-surface effects and cost functions alleviating amplitude mismatching are necessary. A theoretically more appealing approach would be to use elastic modelling to simulate all energies present in the data. However, accurate modelling of the near-surface wavefield and the amplitude of different wave modes is, in itself, a very demanding task. At the moment we feel it probably causes more issues than it solves, not to mention its prohibitive computational cost. While we are investigating this direction further, our current treatment has already shown to be effective for land FWI.

Furthermore, we believe data insufficiency is still a major limiting factor for land FWI on top of the FWI algorithm itself. Land FWI can be more impactful with data consisting of more desirable qualities, such as longer offsets, denser shot and receiver samplings, and higher S/N for low frequencies.

Acknowledgements

We thank CGG Multi-Client & New Ventures for permission to publish this work. We are grateful to our CGG colleagues Weiping Gou, Minshen Wang, and Fengfeng Hou for successfully applying the

method to different land datasets. We also thank Rongxin Huang and Yan Huang for their consistent support in this development.

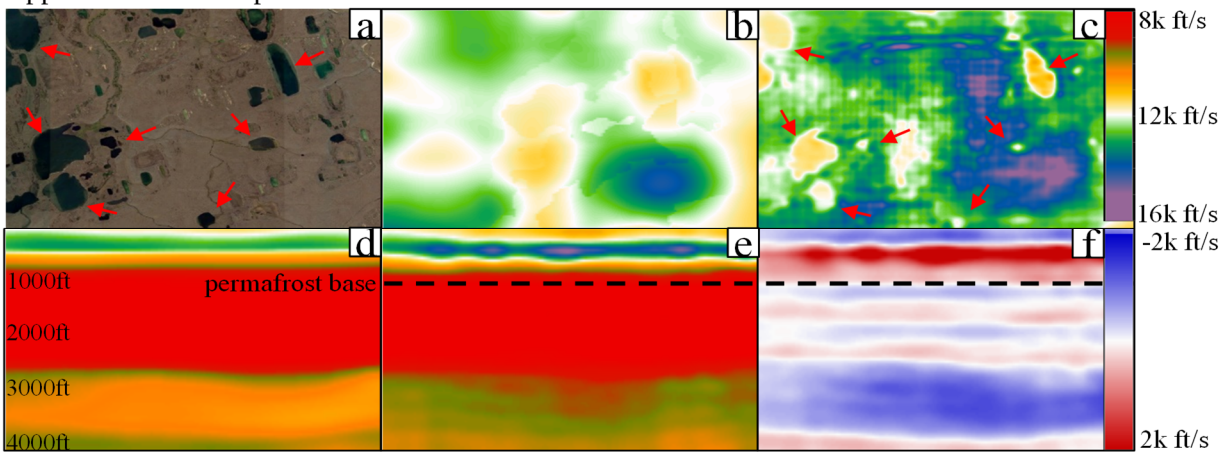

Figure 4 *(a) Satellite image of Tabasco, Alaska survey area; Depth view at 350 ft below topography of (b) initial model, (c) FWI-updated model; Cross-section view of (d) initial model, (e) FWI-updated velocity model, and (f) FWI perturbation.*

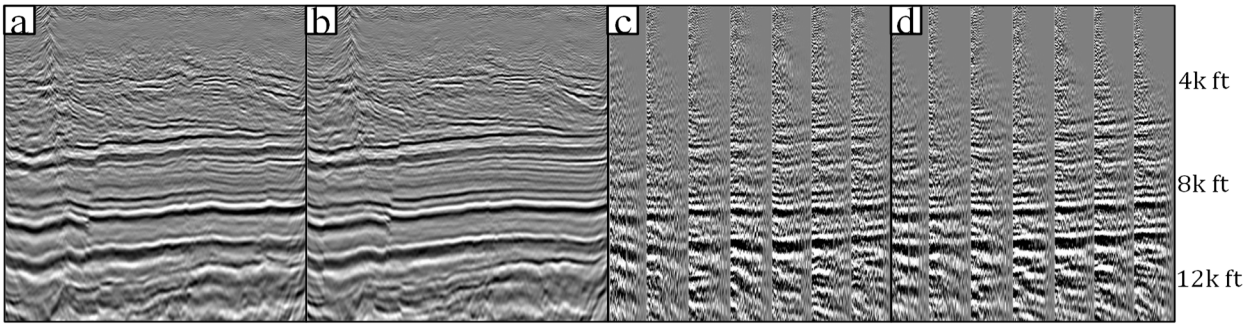

Figure 5 *Stack and gathers from Kirchhoff using (a)/(c) initial model and (b)/(d) FWI-updated model.*

References

Le Meur, D., Benjamin, N., Cole, R. and Al Harthy, M. [2008] Adaptive groundroll filtering. *70th EAGE Conference & Exhibition*, Extended Abstracts, G036.

Mei, J. and Tong, Q. [2015] A practical acoustic full waveform inversion workflow applied to a 3D land dynamite survey. *85th SEG Annual International Meeting*, Expanded Abstracts, 1220–1224.

Plessix, R.E., Baeten, G., de Maag, J.W., Klaassen, M., Rujie, Z. and Zhifei, T. [2010] Application of acoustic full waveform inversion to a low-frequency large-offset land data set. *80th SEG Annual International Meeting*, Expanded Abstracts, 930–934.

Sedova, A., Royle, G.T., Hermant, O., Retailleau, M. and Lambaré, G. [2017] High-resolution land full waveform inversion - A case study on a data set from the Sultanate of Oman. *79th EAGE Conference & Exhibition*, Extended Abstracts, We A3 04.

Shen, X., Ahmed, I., Brenders, A., Dellinger, J., Etgen, J. and Michell, S. [2017] Salt model building at Atlantis with full-waveform inversion. *87th SEG Annual International Meeting*, Expanded Abstracts, 1507–1511.

Shragge, J. [2014] Solving the 3D acoustic wave equation on generalized structured meshes: A finite-difference time-domain approach. *Geophysics*, **79**(6), T363-T378.

Tarantola, A. [1984] Inversion of seismic reflection data in the acoustic approximation. *Geophysics*, **49**(8), 1259-1266.

Wang, D. and Wang, P. [2019] Adaptive quadratic Wasserstein full-waveform inversion. *89th SEG Annual International Meeting*, Expanded Abstracts, 1300-1304.

Wang, P., Zhang, Z., Mei, J., Lin, F. and Huang, R. [2019] Full-waveform inversion for salt: A coming of age. *The Leading Edge*, **38**(3), 304–213.

Zhang, Z., Mei, J., Lin, F., Huang, R., and Wang, P. [2018] Correcting for salt misinterpretation with full-waveform inversion. *88th SEG Annual International Meeting*, Expanded Abstracts, 1143–1147.